
This copy is for your personal, non-commercial use only.

If you wish to distribute this article to others, you can order high-quality copies for your colleagues, clients, or customers by [clicking here](#).

Permission to republish or repurpose articles or portions of articles can be obtained by following the guidelines [here](#).

The following resources related to this article are available online at www.sciencemag.org (this information is current as of April 27, 2014):

A correction has been published for this article at:
<http://www.sciencemag.org/content/304/5676/1449.full.html>

Updated information and services, including high-resolution figures, can be found in the online version of this article at:

<http://www.sciencemag.org/content/304/5669/422.full.html>

Supporting Online Material can be found at:

<http://www.sciencemag.org/content/suppl/2004/04/15/1092905.DC1.html>

This article has been **cited by** 282 article(s) on the ISI Web of Science

This article has been **cited by** 22 articles hosted by HighWire Press; see:

<http://www.sciencemag.org/content/304/5669/422.full.html#related-urls>

This article appears in the following **subject collections**:

Materials Science

http://www.sciencemag.org/cgi/collection/mat_sci

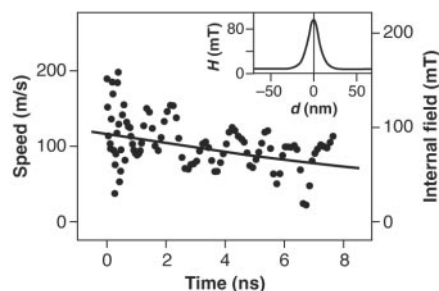


Fig. 3. Vortex speed with respect to the delay time after the field pulse (black dots). The speed was computed from the time-averaged core positions of Pattern I. The solid line is a fit with an exponential function showing a decline in speed, which is the result of damping. The inset shows the simulated profile of the internal field along a cut through the vortex core parallel to the direction of motion.

magnetic fields and moments in a right-handed coordinate system. It does not imply a broken parity. Micromagnetic simulations of the core motion during the first 3 ns are shown in Fig. 2 (B and C) (13). During the external field pulse, the core moves either parallel or antiparallel to the field, depending on the vortex handedness. Afterward, the trajectory turns parallel or antiparallel to the magnetostatic field and the core starts its gyrotropic motion, in agreement with the experiment.

A first estimate of the field H that is driving the vortex motion can be made with the vortex susceptibility χ , which relates the in-plane magnetization density m_d to the field H for a given displacement of the core d , according to $\chi H = m_d = d/l \cdot M_s$. The magnetization density is a linear function of the displacement d , where M_s is the saturation magnetization. We considered a square vortex of length $l = 1 \mu\text{m}$, for which the vortex susceptibility has been determined by simulations to be $\sim 4 \times 10^5$ henries per meter in agreement with experiments (14). For the observed vortex displacement $d = 50 \text{ nm}$, the resulting average internal field is $H = 3 \text{ mT}$. Assuming that this field powers the gyrotropic motion of the vortex center, the speed V of the core can be estimated using $V \approx 2\gamma bH/\pi$. This formula reflects that the precession of core spins by $\pi/2$ corresponds to the translation of the core by its diameter b . γ is the gyromagnetic ratio. Therefore, using $b = 10 \text{ nm}$ (15), we expected a vortex speed of $\sim 4 \text{ m/s}$. However, the experimentally determined vortex speed after the field pulse was close to 100 m/s (Fig. 3). This leads us to the conclusion that the internal field near the core must be considerably higher than the average field estimated with the static susceptibility. By inverting $V \approx 2\gamma bH/\pi$, we translated the measured vortex speed into an experimentally determined local field at the core (Fig. 3, right axis). The size of this

field, $\sim 80 \text{ mT}$, is in good quantitative agreement with the result of a micromagnetic simulation (Fig. 3, inset) (13). The field profile shows a considerably enhanced value at the core that rapidly decreases with increasing distance. This enhanced core field is a consequence of the deformation of the magnetic structure of the vortex core during its gyrotropic motion. Thus, both direction and speed of the nanosecond magnetization dynamics of a vortex are determined by the peculiar structure of the nanometer-scale core.

Accurate measurement of the position and speed of the vortex center thus provides information about the local magnetic fields and the resulting torques in a magnetic pattern on a nanometer scale. The study of picosecond magnetization dynamics on this scale will provide fundamental insight into the properties of mesoscopic magnetic structures, which are the fundamental building blocks of magnetoelectronic devices.

References and Notes

1. T. Shinjo, T. Okuno, R. Hassdorf, K. Shigeto, T. Ono, *Science* **289**, 930 (2000).
2. A. Wachowiak *et al.*, *Science* **298**, 577 (2002).
3. B. E. Argyle, E. Terrenzio, J. C. Slonczewski, *Phys. Rev. Lett.* **53**, 190 (1984).
4. A. R. Volkel, G. M. Wysin, F. G. Mertens, A. R. Bishop, H. J. Schnitzer, *Phys. Rev. B* **50**, 12711 (1994).
5. K. Yu. Guslienko *et al.*, *J. Appl. Phys.* **91**, 8037 (2002).

6. J. P. Park, P. Eames, D. M. Engebretson, J. Berezovsky, P. A. Crowell, *Phys. Rev. B* **67**, 020403 (2003).
7. Y. Acremann *et al.*, *Science* **290**, 492 (2000).
8. Th. Gerrits, H. A. M. van den Berg, J. Hohlfield, K. Bär, Th. Rasing, *Nature* **418**, 509 (2002).
9. J. Stöhr *et al.*, *Science* **259**, 658 (1993).
10. A. Scholl *et al.*, *Science* **287**, 1014 (2000).
11. Materials and methods are available as supporting material on Science Online.
12. A gyrotropic motion in the magnetostatic field of the displaced vortex is superimposed, explaining the angle of the initial acceleration to the external field.
13. Simulations were performed on 20-nm-thick, $1 \times 1 \mu\text{m}^2$ squares divided into 3.3-nm square cells. We used a saturation magnetization of 1.88 T, an exchange stiffness of $3.0 \times 10^{-11} \text{ J/m}$, no crystalline anisotropy, and a damping constant of 0.02.
14. M. Natali *et al.*, *Phys. Rev. Lett.* **88**, 157203 (2002).
15. $b = 2\sqrt{2A/\mu_0 M_s^2}$ approximates core diameter with exchange stiffness A (2).
16. We thank the National Center for Electron Microscopy LBNL and the Microlab at the University of California-Berkeley for giving us access to their lithography facilities and H. C. Siegmann for many valuable discussions. Supported by the Office of Basic Energy Sciences of the U.S. Department of Energy (A.L.S. and S.S.R.L.), by the Laboratory Directed Research and Development Program of LBNL, and by the National Science Foundation under grant no. DMR-0203835 (J.S.).

Supporting Online Material

www.sciencemag.org/cgi/content/full/304/5669/420/DC1

Materials and Methods
Figs. S1 and S2
Movie S1

23 December 2003; accepted 5 March 2004

Ultrahigh Strength and High Electrical Conductivity in Copper

Lei Lu, Yongfeng Shen, Xianhua Chen, Lihua Qian, K. Lu*

Methods used to strengthen metals generally also cause a pronounced decrease in electrical conductivity, so that a tradeoff must be made between conductivity and mechanical strength. We synthesized pure copper samples with a high density of nanoscale growth twins. They showed a tensile strength about 10 times higher than that of conventional coarse-grained copper, while retaining an electrical conductivity comparable to that of pure copper. The ultrahigh strength originates from the effective blockage of dislocation motion by numerous coherent twin boundaries that possess an extremely low electrical resistivity, which is not the case for other types of grain boundaries.

For conducting materials in many applications, high electrical conductivity and high mechanical strength are often required simultaneously. However, pure metals with high conductivities such as Ag, Cu, and Al are very soft. Strengthening the metals via various approaches, including solid solution alloying, cold working, and grain refinement, leads to a pronounced decrease in conductivity.

For example, alloying pure Cu may increase the strength by two or three times, but the electrical conductivity of Cu alloys is only 10 to 40% that of pure Cu (1).

The strength of a solid is determined by the solid's resistance to plastic deformation, and it is sensitive to the solid's chemical composition and microstructure. Plastic deformation of conventional polycrystalline metals is mainly carried by lattice dislocations within individual grains. Several strengthening methodologies have been developed to restrict the dislocation motion. For example, refining grains introduces more grain boundaries (GBs), which are barriers to

Shenyang National Laboratory for Materials Science (SYNL), Institute of Metal Research, Chinese Academy of Sciences, Shenyang 110016, P.R. China.

*To whom correspondence should be addressed. E-mail: lu@imr.ac.cn

intragrain dislocation motion, making the material harder to deform. Solid solution alloying or the introduction of a second reinforcing phase are also effective in forming obstacles to motions of lattice dislocations. Plastic straining also results in hardening, because more dislocations are generated to block further dislocation activities.

All of these strengthening approaches, which are based on the introduction of various kinds of defects (GBs, dislocations, point defects, or reinforcing phases), also increase the scattering of conducting electrons at these defects, thus increasing the electrical resistivity of the metal. For conducting materials, these two essential properties—high electrical conductivity and high mechanical strength—are contradictory (2–4).

The key to making strong but conductive metals is to find an appropriate microstructure in which dislocation motions are effectively blocked while the scattering of conducting electrons is minimized. It is known that a twin boundary (TB), a special kind of coherent boundary, is able to block dislocation motion, like conventional GBs (5, 6), but the electrical resistivity of coherent TBs is about one order of magnitude lower than that of the conventional high-angle GBs (7). Therefore, if it contains a high density of TBs, a metal is expected to be effectively strengthened without losing its high electrical conductivity.

Twin defects are not uncommon in nature and can be formed by various approaches such as plastic deformation, phase transfor-

mation, thermal annealing, and other physical or chemical processes in a large variety of metals and alloys. With these processing techniques, nanotwin structures in bulk forms can be synthesized.

High-purity Cu samples with nanoscale growth twins were synthesized using a pulsed electrodeposition technique from an electrolyte of CuSO_4 (8) [for details, see (9) and table S1]. Transmission electron microscopy (TEM) observations (Fig. 1) indicated that the as-deposited Cu consisted of irregular-shaped grains (most of them were roughly equiaxed in three dimensions) with random orientations (see the electron diffraction pattern in Fig. 1A). The grain sizes were between 100 nm and 1 μm , with an average value of about 400 nm (Fig. 1B). Each grain contained a high density of growth twins of the $\{111\}/[112]$ type. Measurements of the lamella thickness along the $[110]$ orientation showed a wide distribution ranging from several nanometers to about 150 nm (Fig. 1C), due to the fact that in this orientation, only $(\bar{1}11)$ and $(1\bar{1}1)$ twins are edge-on, whereas (111) and $(\bar{1}\bar{1}\bar{1})$ twins are inclined to the surface. The lamella thickness distribution showed a peak at about 15 nm, corresponding approximately to the average lamella thickness for the edge-on twins. The length of twin lamellar geometry varied from about 100 nm to $\sim 1 \mu\text{m}$ (the grain diameter). The high-density growth twins separated submicron-sized grains into nanometer-thick twin/matrix lamellar structures. Close TEM observations and high-resolution TEM images showed that

most TBs were perfectly coherent and atomically sharp (Fig. 1, D and E). Lattice dislocation could not be detected in most lamellae, but a few dislocations were observed in thick lamellae. This agrees with the x-ray diffraction result that a negligible (atomic-level) lattice strain was identified. X-ray diffraction patterns showed an evident (110) texture in the sample, which is consistent with previous observations in electrodeposited Cu specimens with growth twins (10). The thermal stability of the as-deposited Cu sample was studied by examining the twin lamellar structure at elevated temperatures. It was found that thickening of twin lamellae began when the as-deposited sample was isothermally annealed above 250°C (for a duration of 300 s).

The mechanism of twin formation in the electrodeposition product is not fully understood yet. From a thermodynamic point of view, the formation of twins decreases the total interfacial energy, because the excess energy for coherent TBs is much smaller than that for conventional high-angle GBs. Twins prefer to nucleate at GBs or triple junctions (TJs) to reduce the GB energies by means of the twinning-induced orientation change. Although an extra TB is formed, the sum of the interfacial energies (including GBs and TBs) will be reduced by twinning. Twin formation is kinetically driven, and the nucleation and growth rate of twins are controlled by the deposition conditions. Our experimental observations show that when the deposition rate is high (for example, with a high current density or

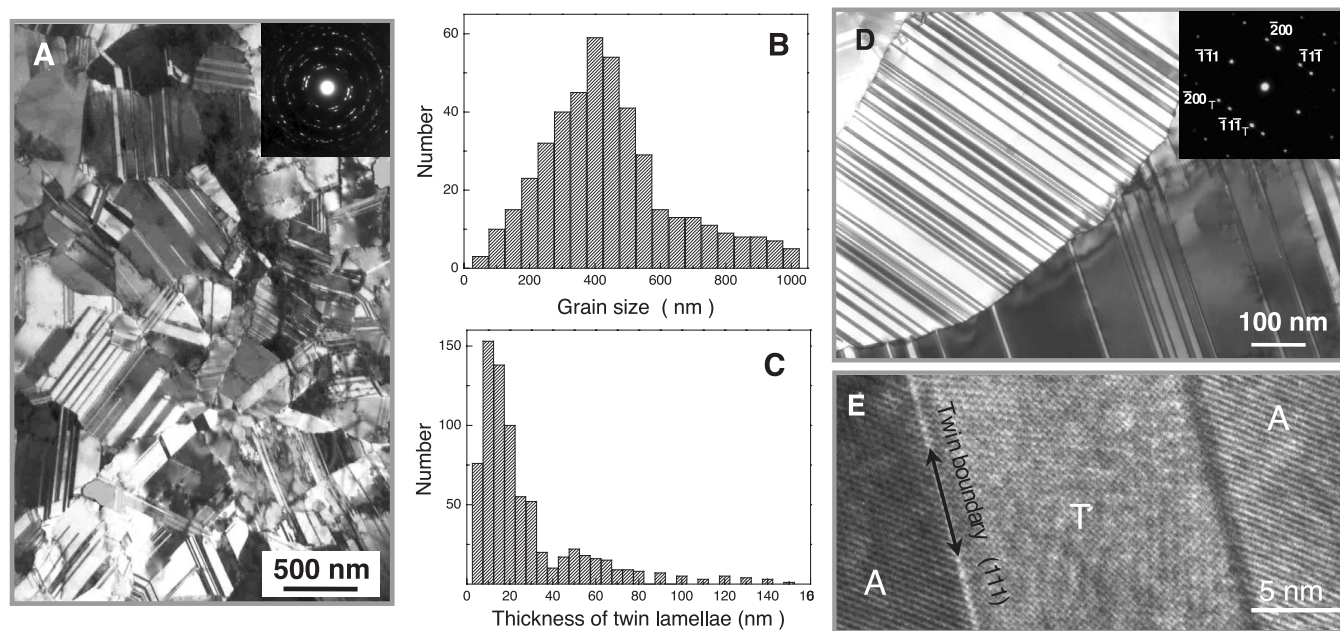


Fig. 1. TEM observations of the typical microstructure in an as-deposited Cu sample. A bright-field TEM image (A) and the electron diffraction pattern (inset) show roughly equiaxed submicrometer-sized grains with random orientations separated by high-angle GBs. The statistical distributions for grain size (B) and for thickness of the twin/matrix lamellae (C)

were obtained from the many TEM images of the same sample. Electron diffraction patterns [inset in (D)] indicate that the twins in each grain are parallel to each other in $\{111\}$ planes (D), and high-resolution TEM images (E) show that the twins follow a sequence of ATATA... with twinning elements, for example, A: $(\bar{1}11)/[112]$ and T: $(111)/[112]$.

a large pH value of the solute) and/or the deposition temperature is low, more twins are formed. This is because with a higher deposition rate and/or a lower temperature, GBs and TJs with higher excess energies will be formed because of the limited relaxation, so that the nucleation rate of twins will be higher to reduce the total interfacial energy. Apparently, the formation of twins is also strongly dependent on the nature of the TBs and the ratio of the TB energy to the GB energy ($\alpha = \gamma_{TB}/\gamma_{GB}$). Large twin densities may be obtained in other metals and alloys with smaller α values (such as those with low stacking fault energies) under proper conditions, such as in cobalt and stainless steels.

In terms of the formation mechanism of twins, pulsed electrodeposition is a technique that is suitable for achieving the nano-twinned structure, whereas conventional direct current (dc) electrodeposition is not. The pulsed electrodeposition process differs from the conventional dc processes mainly in its high peak current density and its on-time and off-time alternatives. The use of the pulse electrodeposition technique permits electrolysis with a very high current density (several orders of magnitude higher than that of dc electrolysis) for a short period of time (0.02 s); that is, a very high deposition rate is achieved during the on time. The Cu^{2+} ion concentration in the vicinity of the cathodes, which is greatly decreased after the high rate of deposition, can be effectively recovered by ion migration for the next pulse of deposition during the relatively long off-time period (2 s). Therefore, pulsed electrodeposition increases the density of nucleation sites because of a high current density during the on time, while interrupting growth and favoring renucleation during the off time, which facilitates the formation of multiple twins.

Tensile tests of the as-deposited Cu foils performed at ambient temperature (9) showed an extremely high strength (Fig. 2A). The tensile yield strength σ_y (at 0.2% offset) reached as high as 900 MPa, and the ultimate tensile strength (σ_{UTS}) was 1068 MPa; these values are at least one order of magnitude larger than those of the coarse-grained (grain size $> 100 \mu\text{m}$) Cu samples that were prepared by annealing the as-deposited Cu sample at 900°C for 10 hours in vacuum. The strength values are higher than those reported for polycrystalline pure Cu with three-dimensional grain sizes down into the nanometer scale (11, 12) (Fig. 2A). The measured elastic strain for this sample is comparable to that of single-crystal Cu whiskers, typically around 1 to 2% (13), which is much higher than that of the coarse-grained form (usually $\sim 10^{-4}$). The Cu sample also showed considerable tensile ductility, with an elongation-to-failure value of 13.5%, which is much larger than that of the previous nanocrystalline Cu specimens with conventional GBs synthesized by means of consolidation of nanometer-sized powders [less than a few percent (14)]. A slight strain hardening appeared in the major plastic deformation stage, indicative of some lattice dislocation accumulation during the plastic straining before failure.

Figure 2B displays the measured temperature dependence of the electrical resistivity (ρ) for the as-deposited Cu sample with nanoscale twins in comparison with the coarse-grained one (9). For both samples, electrical resistivity decreased linearly with the temperature down to about 70 K. Below 70 K, a nonlinear temperature dependence of ρ was detected because of the dominant scattering of grain boundaries in this temperature regime. The electrical resistivity of the nano-

twin Cu sample is very close to that of the coarse-grained Cu specimen over the whole measured temperature range. Repeated measurements gave an electrical resistivity at room temperature ($\rho_{293\text{K}}$) of $1.75 \pm 0.02 \times 10^{-8} \text{ ohm}\cdot\text{m}$ for the nano-twin Cu, in comparison to $1.69 \pm 0.02 \times 10^{-8} \text{ ohm}\cdot\text{m}$ for the coarse-grained one [the literature value is $1.67 \times 10^{-8} \text{ ohm}\cdot\text{m}$ for oxygen-free high-conductivity (OFHC) Cu (2)]. It means that the room-temperature electrical conductivity for the nano-twin Cu was about $96.9 \pm 1.1\%$ of the international annealed copper standard (IACS) (15), which is only about 5% less than that of OFHC Cu (2). The measured temperature coefficient of resistivity at 20°C was $6.78 \pm 0.10 \times 10^{-11} \text{ K}^{-1}$ for the nano-twin Cu and $6.90 \pm 0.10 \times 10^{-11} \text{ K}^{-1}$ for coarse-grained Cu. Both values agree well with the tabulated value of $6.8 \times 10^{-11} \text{ K}^{-1}$ for OFHC Cu (2). The difference in the residual electrical resistivity between the two samples as the temperature approaches 0 K ($\sim 6.8 \pm 1.0 \times 10^{-10} \text{ ohm}\cdot\text{m}$) is an indication of the refined grains (submicrometer-sized) and the ultrafine substructure (nanoscale twin lamellae) in the nano-twin sample. For comparison, the electrical resistivity of a nanocrystalline Cu foil (with conventional GBs and an average grain size of 15 nm) made by means of magneto-sputtering was also measured in the same temperature range (Fig. 2B). The resistivity values in the whole temperature range were at least one order of magnitude higher than that for the nano-twin Cu sample.

Because crystalline defects serve as scattering centers for conduction electrons in metals, increasing their number increases the resistivity. It has been observed experimentally that the total resistivity of a metal (ρ_{total}) is the sum of the contributions from thermal

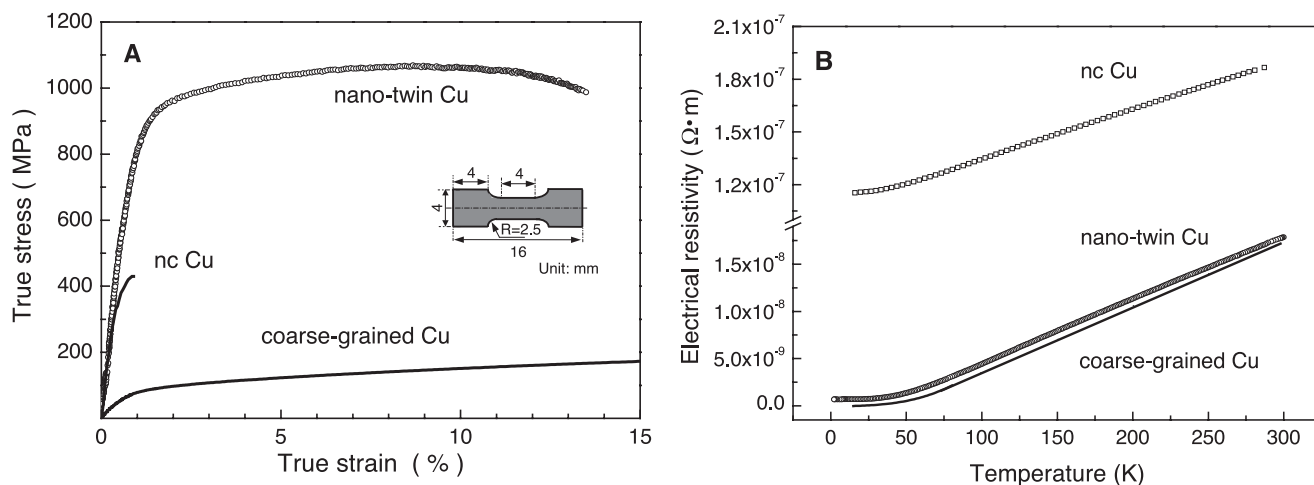


Fig. 2. (A) A typical tensile stress-strain curve for the as-deposited Cu sample with nano-twins in comparison with that for a coarse-grained polycrystalline Cu sample (with an average grain size larger than $100 \mu\text{m}$) and a nanocrystalline (nc) Cu sample (mean grain size $\sim 30 \text{ nm}$) (11). The inset shows the geometry of the tensile sample for the as-deposited nano-twin sample (R ,

radius of curvature). (B) The measured temperature dependence of electrical resistivity (ρ) for the as-deposited nano-twin Cu sample and the coarse-grained sample in a temperature range from 2 to 296 K . For comparison, electrical resistivity measurement results in a nanocrystalline Cu sample with a mean grain size of 15 nm are also included.

vibrations (ρ_t), impurities (ρ_i), and lattice defects such as dislocations and GBs (ρ_d), which is known as Mattiessen's rule, expressed as $\rho_{\text{total}} = \rho_t + \rho_i + \rho_d$.

Comparing the as-deposited Cu sample and the coarse-grained sample, one may see that the only difference in the total resistivity is in the lattice defects term. Because the difference in the lattice dislocation density between the two samples can be neglected, the increment of resistivity in the nano-twin Cu may be attributed to the contributions of GBs and TBs. Room-temperature (295 K) electrical resistivity of GBs in Cu (16) was measured to be about $3.6 \times 10^{-16} \text{ ohm}\cdot\text{m}^2$ and is about $3.4 \times 10^{-17} \text{ ohm}\cdot\text{m}^2$ for stacking faults (17). The resistivity of coherent TBs can be taken as half of the stacking fault specific resistivity (18), which is $1.7 \times 10^{-17} \text{ ohm}\cdot\text{m}^2$ in Cu. By estimating the total GB area and the total TB area in a unit of volume in the nano-twin Cu sample, being approximately $3.8 \times 10^6 \text{ m}^{-1}$ (GB) and $5.0 \times 10^7 \text{ m}^{-1}$ (TB), we found that contributions from these two defects are about $1.4 \times 10^{-9} \text{ ohm}\cdot\text{m}$ and $0.8 \times 10^{-9} \text{ ohm}\cdot\text{m}$, respectively, values that are close to the measured

difference of $0.7 \pm 0.4 \times 10^{-9} \text{ ohm}\cdot\text{m}$. Although the area for TBs is much larger than that for GBs, the contribution of TBs to the increase in resistivity is still minor compared with that of GBs in the present sample. The slight increase in the total resistivity can be mainly attributed to the presence of GBs and a high density of TBs.

To understand the origin of the ultrahigh strength, we modified the deposition parameters to prepare a series of samples with different twin densities, while the average grain sizes, the purity, and the texture remained unchanged. Tensile tests of these samples showed that the strength dropped with a decreasing density of twins (Fig. 3). This provides a direct indication of the strengthening effect of TBs in the Cu sample.

Strengthening metals by means of twins has been studied, and the interaction of glide dislocations with TBs plays an important role. Previous investigations indicated that the presence of twins blocks the propagation of slip bands, implying that existing coherent TBs behave more or less like grain boundaries in acting as obstacles to strain propagation (5). Mechanistic details of the observed behavior have been developed. For example,

considering a case where a $(\bar{1}11)$ slip band interacts with a (111) twin as in the present sample, one may argue that $\frac{1}{2} [01\bar{1}]$ disloca-

tions would propagate across the twin, whereas the motion of $\frac{1}{2} [110]$ and $\frac{1}{2} [101]$

dislocations would be blocked at the TBs. However, these dislocations could also propagate across the twins if they were to undergo dislocation dissociation reactions, such as

$$\frac{1}{2} [101] \rightarrow \frac{1}{6} [1\bar{2}1] + \frac{1}{3} [111].$$

With this reaction, a non-glide Frank dislocation will be left at the TB. Other dislocation reactions are also possible in face-centered cubic metals. Dissociations of dislocation are energetically unfavorable and would require a concentration of stress at twin-slip band intersections, thus leading to strengthening. The strengthening effect of TBs acting as strong barriers to dislocation motion has also been demonstrated in an in situ TEM observation of the deformation process in a nanocrystalline Cu specimen (19). Consequently, twins can be regarded as internal obstacles to the motion of dislocations that may have a strengthening effect analogous to that of GBs (20). The considerable tensile ductility observed in the present Cu sample may be quantitatively attributed to the absorption of a high density of dislocations at TBs, as can be seen in the strained sample under TEM observations.

Figure 4A shows a typical TEM image of the strained sample (after tensile tests), in which plenty of dislocations are identified in contrast with the low dislocation density in the as-deposited sample (Fig. 1D). Close observations indicated that most dislocations were located at TBs, with a spacing ranging from several to several tens nanometers, whereas few were seen inside lamellar layers, as in Fig. 4B. Distributions of dislocations were not uniform, because more dislocations were observed on the TBs separating thick layers and less on those separating thin layers. The inhomogeneous dislocation distribution may originate from the layer thickness effect as well as from different grain orientations. Statistical high-resolution TEM observations in a large area of the deformed sample revealed that most TB disloca-

tions are either Frank dislocations ($\frac{1}{3} [111]$), which are non-glide, as shown in Fig. 4C) or glide Shockley dislocations ($\frac{1}{6} [1\bar{2}1]$). On some

TBs, several Shockley dislocations were found to segregate together, making the TBs curved. These microstructure observations are consistent with the deformation mechanism discussed above, with a dislocation dissociation reaction $\frac{1}{2} [101] \rightarrow \frac{1}{6} [1\bar{2}1] + \frac{1}{3} [111]$. Nevertheless,

Fig. 3. A plot of measured tensile yield strength (σ_y) and ultimate tensile stress (σ_{UTS}) for the as-deposited Cu samples with different twin densities versus the total area of TBs in a unit of volume (S_{TB}) determined from TEM observations.

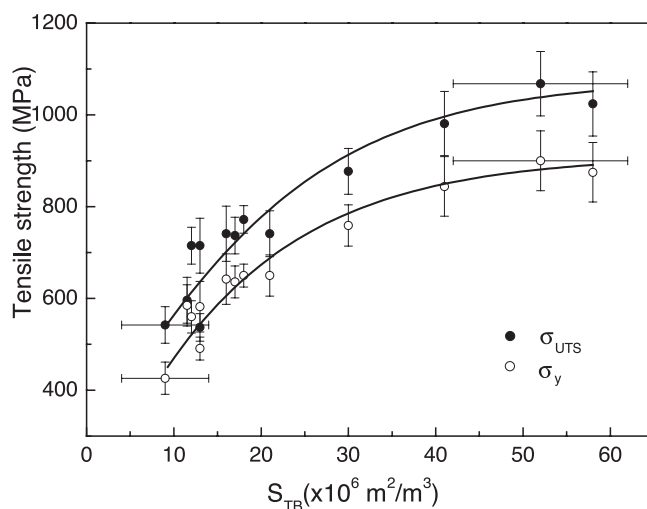
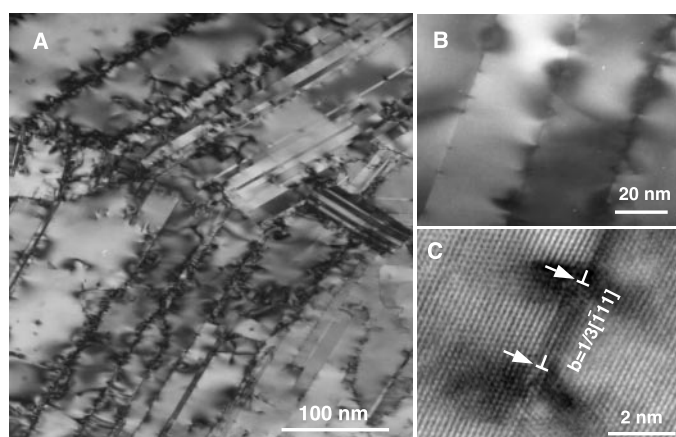


Fig. 4. A typical bright-field TEM image of the strained sample with nanoscale twins after tensile tests (A) and a close observation of the TBs with plenty of dislocations (B). (C) Shows a high-resolution TEM image of a TB with Frank dislocations (b , Burgers vector).



other dislocation reactions cannot be excluded and may also be effective in strengthening. In-depth investigations of the plastic deformation mechanism of the present sample with nano-twins are needed.

The accumulation of dislocation in the sample during plastic deformation is responsible for the obvious work hardening in the tensile stress-strain curve, which may also lead to an increment of resistivity due to more scattering dislocations. The electrical resistivity measurements verified that the room-temperature resistivity was increased by about 11% after the tensile deformation.

References and Notes

1. D. W. Callister Jr., *Materials Science and Engineering, An Introduction* (Wiley, New York, ed. 5, 2000).
2. E. A. Brandes, G. B. Brook, *Smithells Metals Reference Book* (Butterworth-Heinemann, Oxford, 1998).

3. P. V. Anderws, M. B. West, C. R. Robeson, *Philos. Mag.* **19**, 887 (1969).
4. R. H. Pry, R. W. Hennig, *Acta Metall.* **2**, 318 (1954).
5. J. W. Christian, S. Mahajan, *Prog. Mater. Sci.* **39**, 1 (1995).
6. S. D. Dahlgren et al., *Thin Solid Films* **40**, 345 (1977).
7. A. P. Sutton, R. W. Balluffi, *Interfaces in Crystalline Materials* (Clarendon, Oxford, 1995).
8. H. Natter, M. Schmelzer, R. Hempelmann, *J. Mater. Res.* **13**, 1186 (1998).
9. Materials and methods are available as supporting material on Science Online.
10. A. A. Rasmussen, J. A. D. Jensen, A. Horsewell, A. J. Somers, *Electrochim. Acta* **47**, 67 (2001).
11. P. G. Sanders, J. A. Eastman, J. R. Weertman, *Acta Mater.* **45**, 4019 (1997).
12. Y. Wang, M. Chen, F. Zhou, E. Ma, *Nature* **419**, 912 (2002).
13. S. S. Brenner, *J. Appl. Phys.* **27**, 1484 (1956).
14. C. C. Koch, D. G. Morris, K. Lu, A. Inoue, *Mater. Res. Soc. Bull.* **24**, 54 (1999).
15. The IACS is material in which the resistance of a wire 1 m in length and weighing 1 g is 0.15328 ohm at 20°C. The electrical conductivity of the coarse-grained OFHC copper at 20°C is 101.5% IACS.

16. Kh. M. Mannan, Kh. R. Karin, *J. Phys. F Metal Phys.* **5**, 1687 (1975).
17. H. Yoshinaga, *Phys. Stat. Sol.* **18**, 625 (1966).
18. I. Nakamichi, *Mat. Sci. Forum* **207-209**, 47 (1996).
19. C. J. Youngdahl, J. R. Weertman, R. C. Hugo, H. H. Kung, *Scripta Mater.* **44**, 1475 (2001).
20. M. A. Meyers, K. K. Chawla, *Mechanical Behavior of Materials* (Prentice Hall, Upper Saddle River, NJ, 1999).
21. The authors thank the National Natural Science Foundation (grants 50021101 and 50201017), the Ministry of Science and Technology of China (grant G1999064505), and the Max-Planck Society of Germany for financial support; X. Si and H. B. Ma for sample preparation; Z. H. Jin and B. Wu for discussions and TEM experiments; and X. N. Jing for electrical resistivity measurements.

Supporting Online Material

www.sciencemag.org/cgi/content/full/1092905/DC1
Materials and Methods
Table S1

23 October 2003; accepted 5 March 2004

Published online 18 March 2004;

10.1126/science.1092905

Include this information when citing this paper.

Removal of Meteoric Iron on Polar Mesospheric Clouds

John M. C. Plane,^{1*} Benjamin J. Murray,¹ Xinzhaoh Chu,²
Chester S. Gardner²

Polar mesospheric clouds are thin layers of nanometer-sized ice particles that occur at altitudes between 82 and 87 kilometers in the high-latitude summer mesosphere. These clouds overlap in altitude with the layer of iron (Fe) atoms that is produced by the ablation of meteoroids entering the atmosphere. Simultaneous observations of the Fe layer and the clouds, made by lidar during midsummer at the South Pole, demonstrate that essentially complete removal of Fe atoms can occur inside the clouds. Laboratory experiments and atmospheric modeling show that this phenomenon is explained by the efficient uptake of Fe on the ice particle surface.

Polar mesospheric clouds (PMCs), also commonly known as noctilucent clouds, have been intensively studied in recent years because of their potential to provide an early indication of climate change in the upper atmosphere (1), although this remains controversial (2). PMCs consist of ice particles that form through the microphysical processes of nucleation, condensation, and sedimentation (3). They occur when the temperature drops below the water frost point, which is about 150 K in the upper mesosphere (4, 5). The largest ice particles (radius >20 nm) sediment to the base of the cloud layer, where they scatter light sufficiently strongly to be observed by lidar (5, 6) or even with the naked eye during twilight. The meteoric Fe layer peaks at altitudes around 87 km and has

a half-width of about 7 km (7). Thus, if the removal of iron species on the ice particles in a PMC is rapid relative to the input of fresh iron from meteoric ablation, the vertical transport of Fe into the cloud via eddy diffusion, and the lifetime of the cloud itself, then a local depletion or "bite-out" in the Fe density profile should result.

The University of Illinois Fe Boltzmann temperature lidar (8) was installed at the Amundsen-Scott South Pole Station in 1999. This instrument measures the Fe density between about 75 and 110 km. It consists of two lidars operating at the wavelengths of two closely spaced Fe resonance lines (372 and 374 nm). The lidars measure simultaneously the relative populations of the lowest spin-orbit multiplets of ground-state Fe (8). In the presence of a PMC, the lidar return signals consist of resonance backscatter from Fe atoms plus Mie backscatter (the elastic scattering of photons) from the cloud particles. Because the PMC backscatter signals are nearly identical at 372 and 374 nm, whereas the Fe signals are substantially different (the relative

population of the higher multiplet is 1.2% at 145 K), the PMC signal can be eliminated from the 372-nm data by subtracting the 374-nm return signal and scaling the difference. The scaling factor was calculated from the known temperature-dependent relationship of the Fe backscatter signals at 372 and 374 nm (8), assuming the temperature from a South Pole climatology (9). Hence, the Fe density was determined at the altitude of the cloud layer.

Figure 1 shows simultaneous measurements of the atomic Fe and Mie backscatter on 19 January 2000. Note the bite-out in the Fe layer, with essentially complete removal of Fe at the peak of the PMC. These strong bite-outs occur in the period between mid-December and the first week in February, and only when the cloud backscatter brightness exceeds 200 equivalent Fe atoms cm⁻³ (about 10% of the observing time, whereas weaker PMCs are visible for 67% of this period). Another striking feature of the Fe layer in Fig. 1 is that the peak occurs around 92 km, with a density of less than 3000

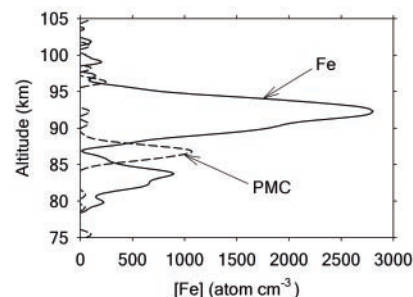


Fig. 1. Simultaneous observations of the atomic Fe density and PMC backscatter signal. The measurements were made with the University of Illinois Fe Boltzmann lidar, operating at 372 and 374 nm, respectively. The signals are averaged between 03:00 and 06:00 UT on 19 January 2000. The PMC backscatter signal is expressed as equivalent Fe atoms cm⁻³ for comparison with the atomic Fe resonance fluorescence signal.

¹School of Environmental Sciences, University of East Anglia, Norwich NR4 7TJ, UK. ²Department of Electrical and Computer Engineering, University of Illinois at Urbana-Champaign, Urbana, IL 61801, USA.

*To whom correspondence should be addressed. E-mail: j.plane@uea.ac.uk